J Mater Sci: Mater Electron **(2023) 34:1703**

Investigation of structural, morphology, and conduction mechanism of GO–Fe_3O_4–TiO_2 composite material

Ayten Ateş[1,*], Khawla ben brahim[2], Neşe Keklikçioğlu Çakmak[1], Abderrazek Oueslati[2], and Mohamed Gargouri[2]

[1] *Department of Chemical Engineering, Engineering Faculty, Sivas Cumhuriyet University, 58140 Sivas, Türkiye*
[2] *Laboratory of Spectroscopic Characterization and Optical Materials, Faculty of Sciences, University of Sfax, B.P. 1171, 3000 Sfax, Tunisia*

Received: 18 May 2023
Accepted: 8 August 2023
Published online: 23 August 2023

ABSTRACT

The graphene oxide composite (GO), iron oxide (Fe_3O_4), and titanium dioxide (TiO_2) were prepared by the sol–gel process. The surface of GO is coated with TiO_2 and Fe_3O_4 nanoparticles, and the composite contains 10.26% C, 23.70% O, 57.17% Ti, and 8.87% Fe. The formation of anatase TiO_2 and magnetite Fe_3O_4 on the surface of GO was detected by XRD and Raman analysis. The N_2 adsorption–desorption isotherm and pore size distribution results showed the formation of a mesoporous material with a specific surface area of 233.3 m^2/g, a total pore volume of 0.298 cm^3/g, and an average pore diameter of 7.7 nm. The GO–Fe_3O_4–TiO_2 composite's dielectric characteristics were examined in the frequency and temperature ranges of 0.1 Hz–5 MHz and 293–373 K, respectively. The Nyquist plot suggests the non-Debye conduction behaviour, which may be related to the distribution of relaxation times within the composite material. The contribution of grains and grain boundaries to the total conductivity is confirmed by impedance spectroscopy. Jonscher's power law was used to examine AC conductivity graphs, and the variation in the exponent "s" revealed that CBH models accurately characterize the conduction mechanism in the composite. The dielectric measurements reveal Maxwell–Wagner polarization and a thermal-activated relaxation process.

1 Introduction

Graphene consists of a layer of carbon atoms and is known as the thinnest conducting layer[1]. The application of a gate voltage can change the properties of the charge carriers from electron-like to hole-like, and extremely high charge carrier mobilities have been recorded [2, 3]. Modification of graphene increases its applications and expands its potential. Derivatives and composites of graphene are used in many different fields such as electronics, electrochemistry, photochemistry, and photocatalysis, due to their unique properties [4–6].

Address correspondence to E-mail: ates@cumhuriyet.edu.tr; aytates@gmail.com

https://doi.org/10.1007/s10854-023-11126-x

Graphene oxide (GO) containing *sp*2 hybridized carbon atoms is prepared by the oxidation of graphite under difficult conditions. When GO with unique properties is combined with metal nanoparticles, their chemical and electronic properties improve significantly. For this purpose, the semiconductor titanium dioxide (TiO_2) is used in various fields, such as catalysts, catalyst supports, and membranes. The electrical properties of TiO_2 have been discussed in the literature by various researchers. For example, TiO_2 is used as a humidity sensor because it reacts differently to different humidity concentrations [7, 8]. The large band gap of bare TiO_2, 3.2 eV for anatase and 3.0 eV for rutile, limits its application for solar light because the recombination of holes (h+) and electrons (e−) is not fast [9]. Therefore, changes in morphology must be made by coupling TiO_2 with other noble metals, nonmetals, semiconductors, etc., to improve photocatalytic activity along with electrical conductivity. For this purpose, TiO_2 can be anchored to GO which has excellent electrical conductivity, is rich in hydrophilic oxygen-containing functional groups, and has high chemical stability [10, 11].

Magnetite (Fe_3O_4) consists of equivalent trivalent and divalent iron ions (Fe^{3+} and Fe^{2+}) and is used in many applications. Comparing Fe_3O_4 with other iron oxides, it is found that its higher light absorption allows for high electrocatalytic activities and high performance in solar cells [12, 13]. Therefore, anchoring Fe_3O_4 with GO together with TiO_2 allows the formation of materials with unique properties.

Based on the forementioned explanations, the main objective of this study is to study the structural, morphological, and conductive properties of the GO anchored in the TiO_2 and Fe_3O_4. GO–Fe_3O_4–TiO_2 composite. The latter was prepared using GO synthesized by the Hummers method [14] with sol–gel synthetise technic. The composite was characterized using XRD, SEM-EDS, N_2 adsorption–desorption, and Raman spectroscopy. Moreover, the dielectric and electrical properties are investigated in the current work through impedance spectroscopy measurements as a function of temperature and frequency.

2 Experimental

2.1 Materials and methods

Graphene oxide (GO) was synthesized from graphene powder using a modified Hummers method [14]. Fe_3O_4 nanoparticles were prepared by thermal decomposition of $FeSO_4$ and $FeCl_3$ in ethylene glycol (EG) with sodium acetate (NaAc) and ethanolamine[15]. A composite material of Fe_3O_4, GO, and TiO_2 was prepared by sol–gel method as reported in our previous study [16]. Fe_3O_4 and GO were dried at 60 °C for 24 h before the sol–gel method. To prepare the composite, 0.65 g of GO and 0.65 g of Fe_3O_4 were dissolved separately in 260 mL of ethanol and sonicated for 1 h. After mixing both solutions, 65 mL of titanium (IV) butoxide was added and mixed for 1 h. The mixture was heated in a Teflon-coated stainless-steel autoclave under nitrogen purge for 10 h at 180 °C. After the reaction, the grey coloured precipitate was washed with ethanol and water to remove impurities and dried at 60 °C for 10 h in a vacuum oven. The composite was labelled as GO–Fe_3O_4–TiO_2.

2.2 Characterizations

X-ray diffraction (XRD) of the composite material was measured using Panalytical Empyrean Diffractometer (Malvern Panalytical Ltd., Malvern, UK) with Cu Kα (λ = 1.54 Å).

A scanning electron microscope (SEM) of the GO and GO–Fe_3O_4–TiO_2 was visualized with TESCAN MIRA3 XMU to reveal the surface morphology of the nanocomposite.

Raman spectra of the composite were measured using a micro-Raman system (Renishaw inVia Qontor, UK) equipped with a 785 nm laser.

The N_2 adsorption–desorption isotherm to determine the surface and pore properties of GO and GO–Fe_3O_4–TiO_2 wasdetermined using the AUTOSORB 1 C sorption analyzer (Quantachrome Corp., USA). Nitrogen with a purity of 99.99% was used as adsorption gas. Multipoint BET (Brunauer–Emmett–Teller) and *t*-plot techniques, were used to calculate the surface area and pore volume. Using the Barrett, Joyner, Halenda (BJH) approach based on the Kelvin equation, the distribution of pore sizes was determined. With P/P^o = 0.99, the total pore volume (V_T) was assumed to be the adsorbed volume, with adsorption and desorption occurring simultaneously. The Autosorb 1 C package program was used for the calculations.

The impedance spectroscopy measurements on the GO–Fe_3O_4–TiO_2 composite material were carried out on disc shaped pellets (8 mm diameter and 1.2 mm thickness) in a uniaxial hydraulic press at a pressure of 3 tons/cm^2. The pellet was prepared with a relative density of 92%. Then, thin gold films,

(with a thickness of a few nanometers), were manually deposited on both flat faces of the pellet. This measurement was performed using an Impedance/Gain-Phase analyzer (Solartron SI-1260), coupled with a dielectric interface (Solartron 1296), and a temperature control system (Linkam LTS420). The data were collected at temperatures between 293 and 393 K over a wide frequency range from 10^{-1} to 5 MHz.

3 Results and discussion

3.1 X-ray diffraction analysis

The XRD pattern of GO–Fe_3O_4–TiO_2 is shown in Fig. 1. In the XRD analysis with MDI Jade 6, the sample mainly contains the anatase phase of TiO_2 (PDF: 73-1764) and the magnetite phase (PDF: 75-0033) of iron oxide. The estimated crystal size of the material was calculated to be 56 (11) Å. The characteristic peak index of TiO_2 and Fe_3O_4 was marked in Fig. 1. Since the anatase peak of TiO_2 at 25.5° coincides with reduced graphene oxide [17, 18], the characteristic peak of reduced graphene oxide cannot be detected in Fig. 1.

3.2 Scanning electron microscope analysis

The elemental composition of GO, determined by EDS, is 56.2% C and 43.8% O. After preparation of a composite of Fe_3O_4, GO, and TiO_2, the material contains 10.26% C, 23.70% O, 57.17% Ti, and 8.87% Fe. The SEM images in Fig. 2 show a comparison of GO and GO–Fe_3O_4–TiO_2. The GO has a smoother surface with layered structure. When Fe_3O_4 and TiO_2 were added to GO, Fe_3O_4 and TiO_2 nanoparticles accumulated on the surface of GO. Also GO–Fe_3O_4–TiO_2 particles with agglomerated and irregular structures are formed.

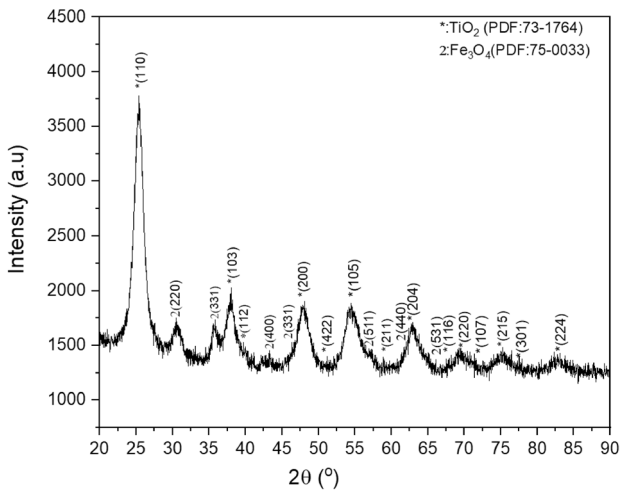

Fig. 1 XRD diffraction pattern of GO–Fe_3O_4–TiO_2

3.3 Vibrational spectroscopy study

An effective method for examining the arrangement of crystal structures in carbonaceous materials is Raman spectroscopy. The Raman spectral curve of GO and GO–Fe_3O_4–TiO_2 is shown in Fig. 3. Two distinctive peaks of GO can be seen at 1350 and 1591 cm^{-1}, which correspond to the D band and G band, respectively. The D band in disordered carbon indicates structural defects. However, in *sp*2 carbon domains, the G band is the E_{2g} vibrational mode of first-order scattering [19]. The disorder of carbon is often related to the intensity ratio (I_D/I_G). The intensity ratio of I_D/I_G for GO is 0.978. The peaks of GO–Fe_3O_4–TiO_2 are observed at 1345 cm^{-1} and 1598 cm^{-1} with 0.983 of I_D/I_G. The introduction of Fe_3O_4–TiO_2 into GO increases the value of I_D/I_G, indicating increasing *sp*3 defects in the *sp*2 due to the formation of GO–Fe_3O_4–TiO_2. The peak at 154 cm^{-1} is related to the anatase phase of TiO_2 [20] along with the peaks at 537 and 647 cm^{-1} [21]. The peaks at 212, 285 and 402 cm^{-1} show the presence of Fe_3O_4 [22].

3.4 N_2 adsorption–desorption isotherm

The N_2 adsorption–desorption isotherms and pore size distributions of GO–Fe_3O_4–TiO_2 are shown in Fig. 4a. The hysteresis observed in the range of 0.4–0.95 P/Po shows the opening between the plates. The isotherm of the composite corresponds to the IV type with a hysteresis loop of H_4, which is characteristic of micro-mesoporous materials [23]. The surface area and pore volume of the composite were calculated to be 233.3 m^2/g and 0.298 cm^3/g, respectively. According to the BJH method, the average pore size of GO–Fe_3O_4–TiO_2 is 7.7 nm, as shown in Fig. 4b. As a result, the prepared composite material has a mesoporous structure with high surface area.

3.5 Electrical conductivity

To investigate the electrical properties of materials, impedance spectroscopy is a commonly used

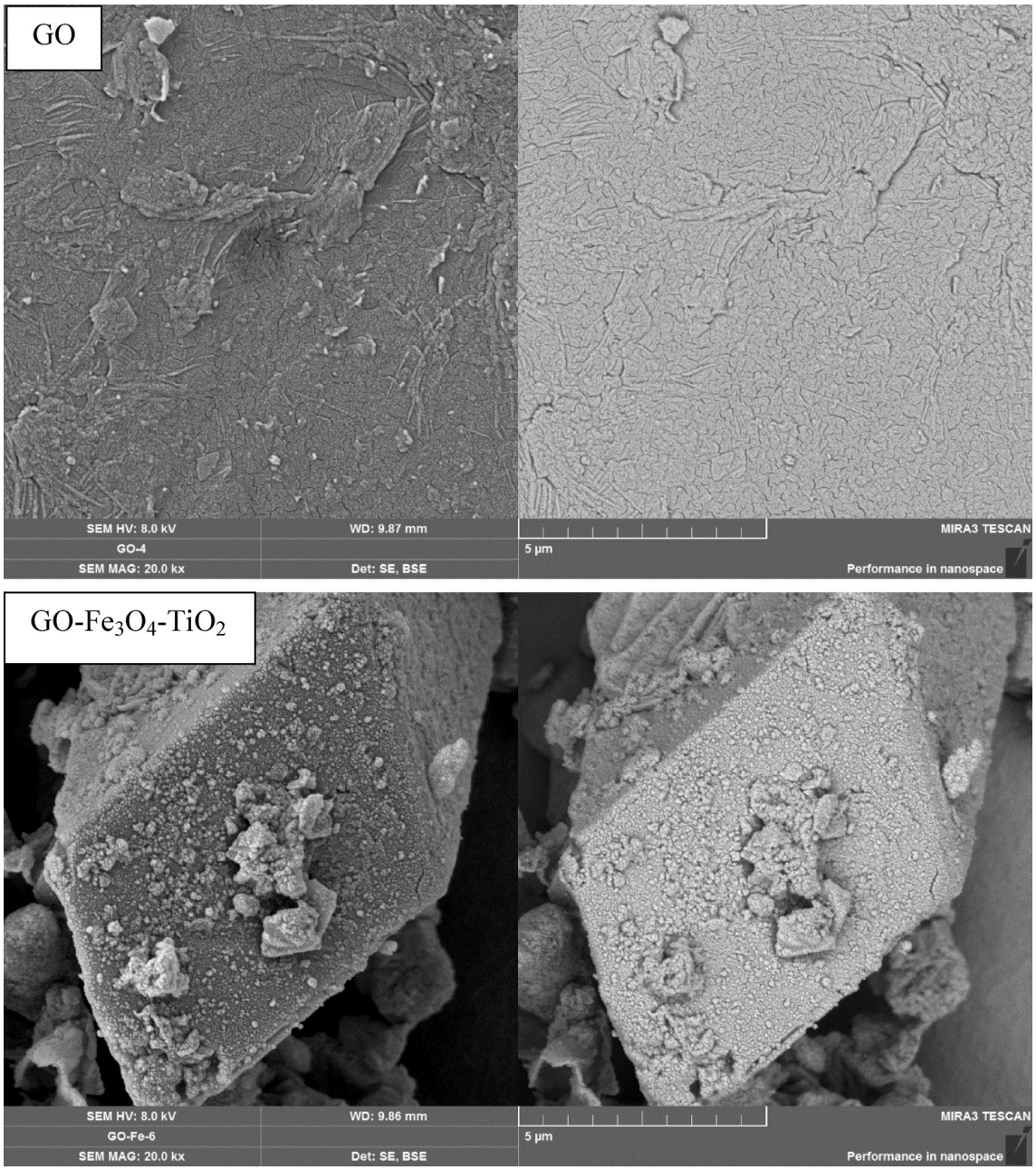

Fig. 2 SEM pictures of GO and GO–Fe_3O_4–TiO_2

technique in electrochemistry and materials research. It is feasible to glean knowledge about the dynamics of the charges within the material as well as the mechanisms governing charge transport by studying the frequency-dependent impedance [24].

Figure 5 depicts the evolution of the real impedance (Z') against frequency for the GO–Fe_3O_4–TiO_2 composite. The fact that Z' values decrease as temperatures increase points to a material that is more electrically conductive. This behaviour is frequently accompanied by a negative temperature coefficient of resistance (NTCR), which has also frequently been noted in earlier investigations [25, 26]. The increase in electrical conductivity with temperature can be attributed to an increase in the mobility of charge carriers in the material [27]. The existence of dc conductivity is then

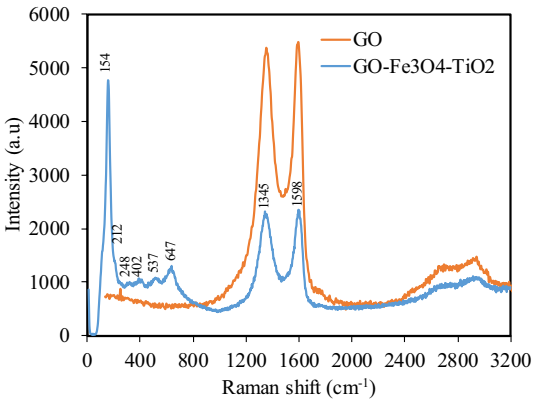

Fig. 3 Raman spectrum of GO and GO–Fe_3O_4–TiO_2

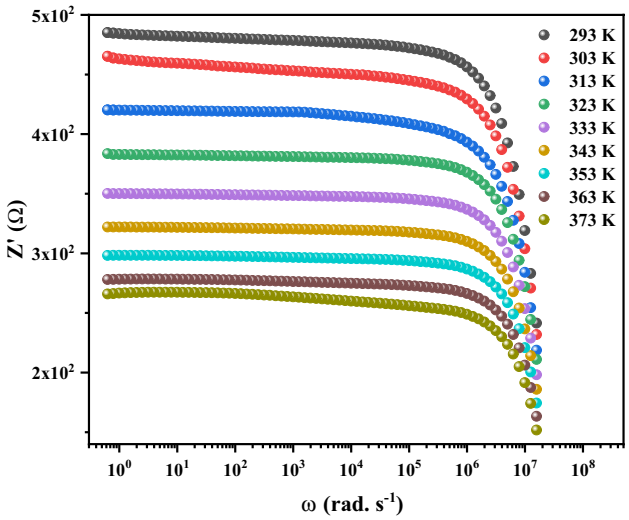

Fig. 5 Variation of real part of the impedance (Z') as a function of frequency and different temperatures

predicted by the observation of constant values for Z' at low frequencies ($< 10^5$ rads^{-1}), which is also clearly seen [28]. The Z' values rapidly go off at high frequencies. According to this behaviour, the produced material may have ac conductivity [28].

Figure 6 illustrates the temperature-dependent frequency response of Z'' for the GO–Fe_3O_4–TiO_2 composite, which provides valuable information about the relaxation behaviour of the material. At all temperatures, two peaks are observed in the plot, indicating the presence of two relaxation processes in the material.

The initial peak observed at low frequencies is attributed to the grain boundary relaxation process, which is associated with the movement of charged defects or ions along the grain boundaries. As temperature increases, the mobility of these defects or ions also increases, leading to a shift in the frequency at which the peak occurs to higher frequencies. The reason behind this displacement may be due to the accumulation of charge carriers [29]. Also, the broadening

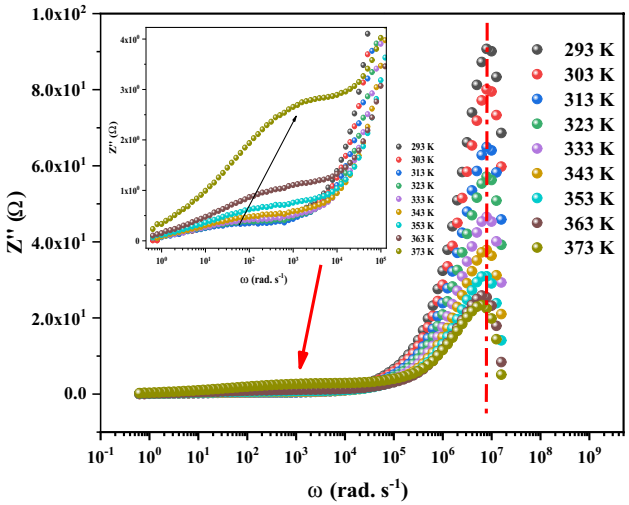

Fig. 6 Variation of imaginary part of the impedance Z'' as a function of frequency and at different temperatures

Fig. 4 N_2 adsorption-desorption isotherm (**a**) and pore size distribution (**b**) of GO–Fe_3O_4–TiO_2

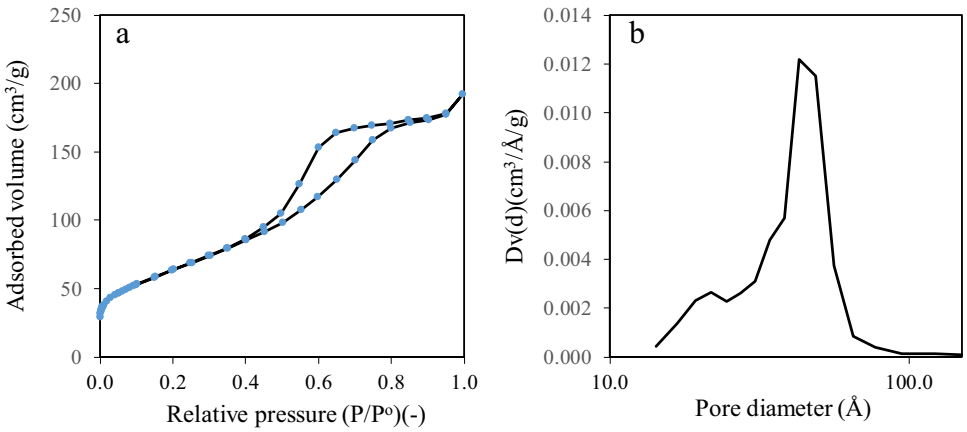

in the peaks verified the temperature dependence on the electrical relaxation mechanism in the material [30].

The second peak observed at higher frequencies corresponds to the grain relaxation process, which is associated with the movement of charged defects or ions within the grains. This process is less sensitive to temperature, and hence the frequency at which the peak occurs remains constant with increasing temperature.

The Nyquist plot is graphical representations of the impedance data, with Z'' (the imaginary part of the impedance) plotted against Z' (the real part of the impedance). This plot can provide information about the distribution of relaxation times and the charge transport mechanisms in the material [31]. In the case of the GO–Fe_3O_4–TiO_2 composite, Fig. 7 present the variation of Z'' against Z' (Nyquist plot) in the temperature range of 293–373 K. The presence of depressed semicircle at all temperatures indicates the presence of a distribution of relaxation times, which can be associated with non-Debye conduction processes in the material [32]. The decreasing radius of the semicircle with increasing temperature suggests a change in the dynamics of the charges within the material, such as an increase in the mobility of charge carriers, and that conductivity is a thermally activated process [32]. The Nyquist plot described by a attened arc with its center located below the real axis arc, at each temperature, may be related to the grain and grain boundary contribution in this material [33].

The frequency dependence of the electrical conductivity is a commonly used method to study the active conduction process in materials. It can provide insight into the types of charge carriers present and the mechanisms governing charge transport. By measuring the conductivity at different temperatures, it is also possible to determine the activation energy for charge transport. The total conductivity values are determined from the impedance measurements according to the following expression [34]:

$$\sigma = \frac{e}{S} \times \frac{Z'}{Z'^2 + Z''^2} \quad (1)$$

The behaviour of the frequency response of the ac conductivity of the investigated composite is shown in Fig. 8. When a range of practically frequency-independent conductivity appears in the low frequency zone, it means that the frequency of the applied electric field has little effect on the material's charge carriers. Dc conductivity is matched by this plateau. However, electrical conductivity is substantially temperature dependent in such a plateau. This behaviour suggests that the conduction mechanism in the material is thermally activated [35]. The ac conductivity, which characterizes the dispersion phenomenon and increases with increasing frequency, manifests in the high frequency zone [36].

To determine the appropriate conduction mechanism in the GO–Fe_3O_4–TiO_2 composite, we fitted total conductivity data using Jonscher's law, which

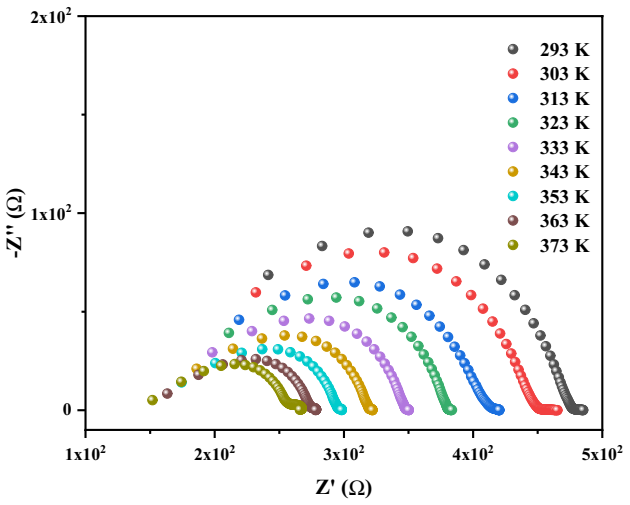

Fig. 7 Nyquist diagram of GO–Fe_3O_4–TiO_2 composite as a function of temperature

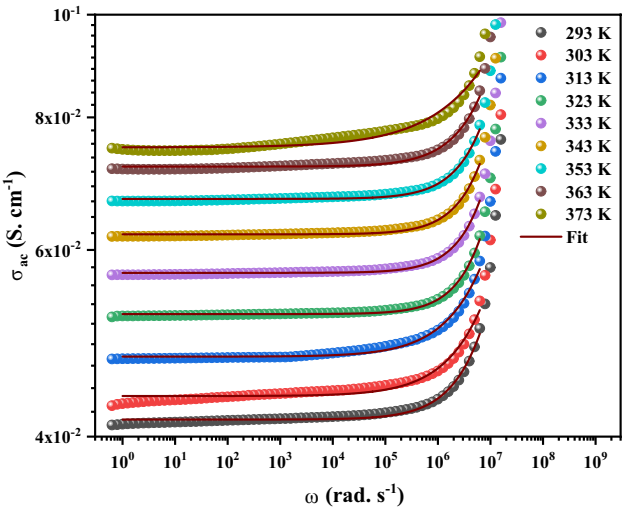

Fig. 8 Plots of σ_{ac}–log(ω) of the GO–Fe_3O_4–TiO_2 composite in various temperatures

is a widely used empirical relation that describes the frequency-dependent conductivity described by the following [37]:

$$\sigma_T(\omega) = \sigma_{DC} + A\omega^s = \sigma_{DC} + \sigma_{AC}, \quad (2)$$

where $\sigma_T(\omega)$ is the total conductivity at frequency ω, s is the degree of interaction between mobile ions with the lattices around them and A is a constant whose value specifies the strength of polarizability.

It was possible to determine the parameter 's' at various temperatures by modelling the experimental curves using the Jonscher equation (Eq. 2), which demonstrates good agreement between the theoretical and experimental curves. Analysis and comparisons with theoretical models are done for thermal evolution of the exponent 's' (Fig. 9) [38]. It is clear that the value of s decreases with increasing temperature. This result suggests that the CBH model is the best choice for characterizing the electrical conduction process [39]. Where, the CBH conduction mechanism involves charge carrier hopping between closed sites over a potential barrier that separates them [40].

Figure 10 displays the relationship between ac conductivity and the temperature inverse for various frequencies. The experimental data can be fitted using the first-order Arrhenius law to determine the material's activation energy E_a. Based on the assumption that thermally activated hopping between localized states dominates the conduction mechanism, this model depicts the temperature dependence of the electrical conductivity of materials caused by thermally activated carriers [36].

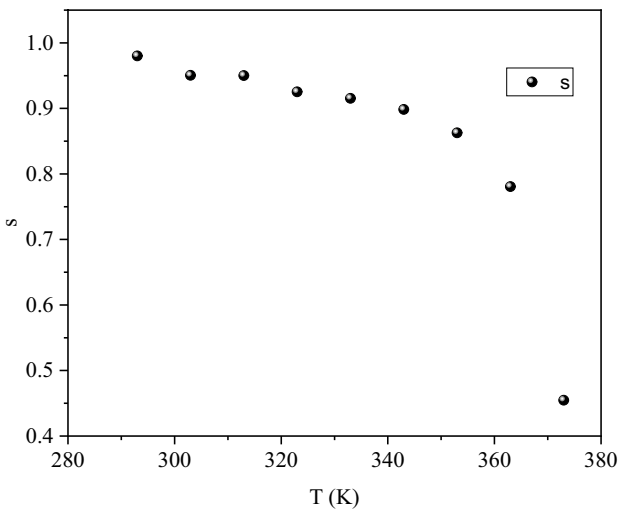

Fig. 9 The thermal evolution of exponent s

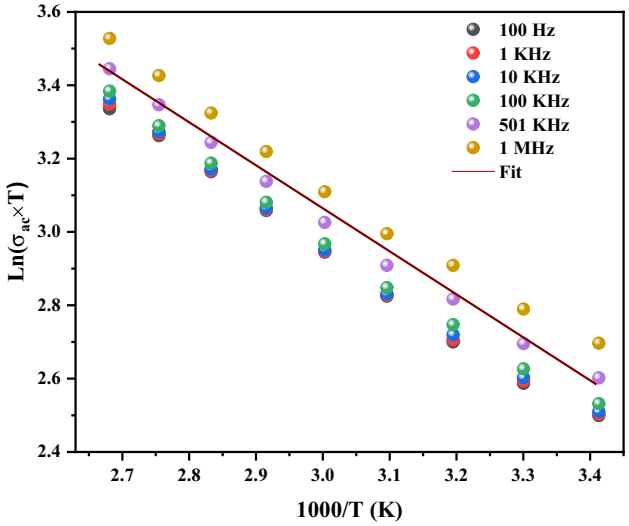

Fig. 10 Plots of Ln (σ_{ac}, T) versus 1000/T at different frequencies

$$\sigma_{ac}T = \sigma_0 \exp\left(-\frac{E_a}{k_B T}\right), \quad (3)$$

where $\sigma(T)$ is the electrical conductivity at temperature T, σ_0 is a pre-exponential factor that depends on the material and the density of states at the Fermi level, E_a is the activation energy (required for a charge carrier to hop from one localized state to another), k_B is the Boltzmann constant, and T is the absolute temperature.

The activation energy deduced from each linear side's slope is E_a = 0.10 eV. It suggests that the charge carriers can easily hop between localized states with a relatively low amount of energy. This indicates that the material may have a high density of localized states, or the localized states may be relatively shallow.

3.6 Dielectric study

Different types of polarization, such as electronic polarization, ionic polarization, dipole orientation polarization, and space charge polarization, can affect a material's overall dielectric response. Dielectric properties are connected to how a material reacts to an applied electric field. By examining the dielectric response with frequency and temperature, it is possible to identify the

relative contributions made by each of these polarization types to the material's dielectric response.

The complex dielectric constant, also called the complex permittivity, is a complex-valued number that explains how a material interacts with an electric field at a specific frequency. It is denoted by the following [41]:

$$\epsilon^*(\omega) = \epsilon' - i\epsilon'', \tag{4}$$

where ε' is the real part of the dielectric constant, which represents the energy stored in the electric field, and ε'' is the imaginary part of the dielectric constant, which represents the energy dissipated as heat by the material.

Figure 11 exposes the variation of real permittivity ε' with frequency at various temperatures. The figure shows that the dielectric constant has massive values, particularly at low frequencies, and that as the frequency rises, the values of the dielectric constant rapidly decrease. Four main types of polarization, including electronic, ionic, orientational, and space charge polarization, each contribute to the observation of maximum dielectric constant values at the low frequency area [42]. Real permittivity increases with temperature, illustrating that charge carriers are thermally activated. The two-layer Maxwell–Wanger model [43] explains how the dielectric permittivity evolved. We suppose that the material is made up of two layers, with the grains having a high conductivity and the grain boundaries having a low conductivity. At lower frequencies the grain boundaries possess high resistance, so the electrons gather and generate polarization at the boundaries which explains the dielectric behaviour of the material in the low frequency area. Thereafter, we see an abrupt drop in the dielectric constant that is independent of temperature. This may be explained by the fact that when frequency increases, electrons move in the opposite direction, which reduces polarization.

Figure 12 shows the evolution of imaginary permittivity with frequency at various temperatures. It is observed that the imaginary permittivity rapidly declines with frequency, and at low frequencies, there is a high value of ε'' that can be connected to the presence of space charge polarization at the interfaces of grain boundaries [44]. The Wagner and Koop model, which claims that at low frequencies, well-conductive grains are separated by very resistive grain boundaries, causes the polarization of the space charge, explains this behaviour of the imaginary permittivity with frequency. The material can store a lot of electrical energy, as evidenced by the high value of ε'' at low frequency, making it useful for applications such as capacitors. The ability of the charge carriers to move in response to the electric field decreases as the frequency rises, which causes a reduction in polarization and a corresponding fall in the imaginary permittivity. The dielectric permittivity's temperature-dependent development suggests that charge carriers are thermally activated.

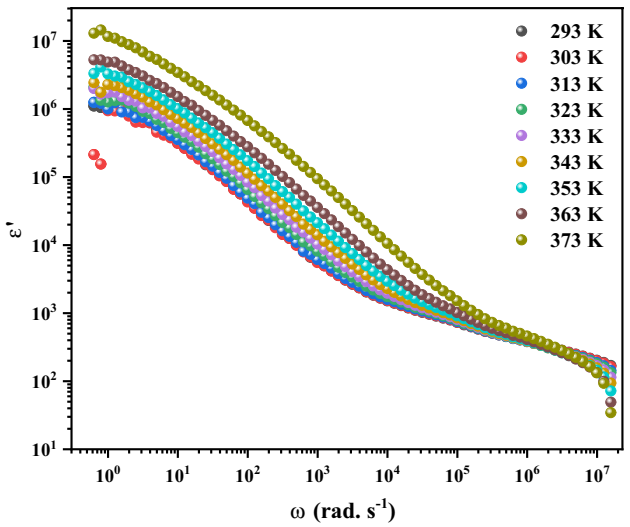

Fig. 11 Variation of real part of dielectric permittivity as a function of frequency at different temperatures

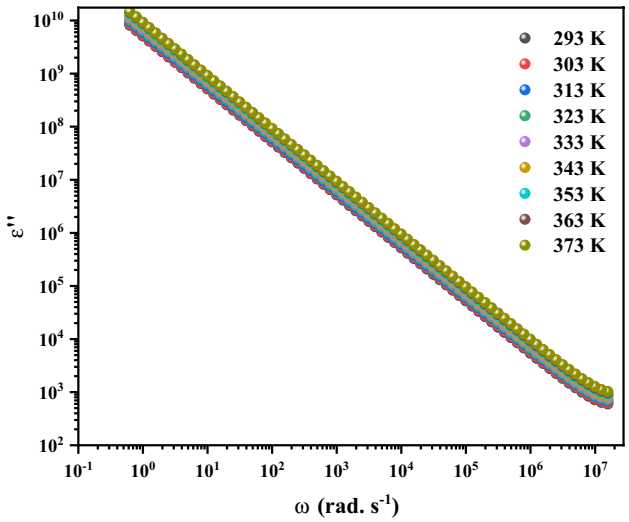

Fig. 12 Variation of imaginary part of dielectric constant with frequency at different temperatures

4 Conclusion

A composite material was prepared by precipitating iron oxide and titanium oxide on the graphene oxide (GO) surface. The characterization results showed that anatase TiO_2 and magnetite Fe_3O_4 particles were formed on the graphene oxide surface. The investigation of the surface and pore properties showed that the composite material has a mesoporous structure and has a surface area of 233.3 m^2/g and a total pore volume of 0.298 cm^3/g.

The GO–Fe_3O_4–TiO_2 composite's dielectric characteristics were examined and Nyquist plots of the material demonstrated the existence of grains and the contribution of grain boundaries, as well as a thermally activated conduction mechanism. It turned out that the AC conductivity spectrum follows Jonscher's power law. The correlated barrier hopping (CBH) model was found to be the most appropriate one based on the temperature dependency of the exponents s(T). The dielectric constant declines with frequency before stabilizing at a low value that represents typical dielectric dispersion, according to data on its variation with frequency and temperature. The GO–Fe_3O_4–TiO_2 composite exhibits a high value of ε'' at low frequencies, indicating that it will have a large capacity to store electrical energy, making it ideal for capacitor applications. Therefore, the material is able to resist the flow of current, and it can hold a charge for a longer period of time.

Author contributions

All authors contributed to the study conception and design. Material preparation, data collection and analysis were performed by NKÇ, KBB and AA. The writing of the manuscript was written by AA, AO and MG and all authors commented on previous versions of the manuscript. All authors read and approved the final manuscript.

Funding

The authors have not disclosed any funding.

Data availability

Not applicable.

Declarations

Competing interests The authors have no competing interests to declare that are relevant to the content of this article.

Ethical approval Not applicable.

References

1. A.K. Geim, K.S. Novoselov, J. Nat. Mater. (2007). https://doi.org/10.1038/nmat1849
2. J.H. Chen, C. Jang, S. Xiao, M. Ishigami, M.S. Fuhrer, J. Nat. Nanotechnol. (2008). https://doi.org/10.1038/nnano.2008.58
3. K.S. Novoselov, A.K. Geim, S.V. Morozov, D. Jiang, Y. Zhang, S.V. Dubonos, I.V. Grigorieva, A.A. Firsov, J Sci. (2004). https://doi.org/10.1126/science.1102896
4. S. Uruş, M. Çaylar, H. Eskalen, Å. Özgan, J. Mater. Sci. Mater. Electron. (2022). https://doi.org/10.1007/s10854-021-07625-4
5. M. Zangiabadi, T. Shamspur, A. Saljooqi, A. Mostafavi, J. Appl. Organomet. Chem. (2019). https://doi.org/10.1002/aoc.4813
6. A.M. Haji, A. Hossein, A. Samadi, J. Mater. Sci. Mater. Electron. (2022). https://doi.org/10.1007/s10854-022-07777-x
7. H. Lensch, J. Doerr, A. Schütze, T. Sauerwald, J Sens. Actuators B Chem. (2020). https://doi.org/10.1016/j.snb.2020.128497
8. M. Morsy, A. Elzwawy, A.I. Abdel-Salam, M.M. Mokhtar, A.B. El Basaty, J. Diam. Relat. Mater. (2022). https://doi.org/10.1016/j.diamond.2022.109040
9. S. Gonuguntla, S. Sk, A. Tiwari, H. Mandal, P.N. Lakavath, V. Perupoga, U. Pal, J. Mater. Sci. Mater. Electron. (2021). https://doi.org/10.1007/s10854-021-05848-z
10. S. Bai, M. Yang, J. Jiang, X. He, J. Zou, Z. Xiong, G. Liao, S. Liu, J. 2D Mater. Appl. (2021). https://doi.org/10.1038/s41699-021-00259-4
11. M. Yang, Y. Zou, L. Ding, Y. Yu, J. Ma, L. Li, A.F. Rafryanto, J. Zou, H. Wang, J. Carbon Lett. (2023). https://doi.org/10.1007/s42823-022-00456-1
12. J.-C. Chou, C.-M. Chu, Y.-H. Liao, C.-H. Lai, Y.-J. Lin, P.-H. You, W.-Y. Hsu, C.-C. Lu, Y.-H. Nien, J. IEEE Electron. Devices Soc. **5**, 32 (2016). https://doi.org/10.1109/JEDS.2016.2618839
13. V. Harnchana, S. Chaiyachad, S. Pimanpang, C. Saiyasombat, P. Srepusharawoot, V. Amornkitbamrung, J. Sci. Rep. (2019). https://doi.org/10.1038/s41598-018-38050-z

14. D.C. Marcano, D.V. Kosynkin, J.M. Berlin, A. Sinitskii, Z. Sun, A. Slesarev, L.B. Alemany, W. Lu, J.M. Tour, ACS Nano (2010). https://doi.org/10.1021/nn1006368
15. A. Angermann, J. Töpfer, J. Mater. Sci. (2008). https://doi.org/10.1007/s10853-008-2738-3
16. N.K. Cakmak, Z. Said, L.S. Sundar, Z.M. Ali, A.K. Tiwari, J. Powder Technol. (2020). https://doi.org/10.1007/s10853-008-2738-3
17. M.A. Baghchesara, H.R. Azimi, A.G. Shiravizadeh, M.A.M. Teridi, R. Yousefi, J. Appl. Surf. Sci. (2019). https://doi.org/10.1016/j.apsusc.2018.10.082
18. V.S. Sumi, M.S. Meera, M.A. Sha, S.M.A. Shibli, J. Hydrog. Energy (2020). https://doi.org/10.1016/j.ijhydene.2019.11.167
19. A.C. Ferrari, D.M. Basko, Nat. Nanotechnol. **8**, 235 (2013)
20. H.D. Ngoc, D.M. Xuan, T.M. Van, Catalysts. **10**, 1 (2020)
21. J.C. Parker, R.W. Siegel, J. Mater. Res. (1990). https://doi.org/10.1557/JMR.1990.1246
22. S. Banerjee, P. Benjwal, M. Singh, K.K. Kar, Appl. Surf. Sci. (2018). https://doi.org/10.1016/j.apsusc.2018.01.085
23. R. Bardestani, G.S. Patience, S. Kaliaguine, J. Can. J. Chem. Eng. (2019). https://doi.org/10.1002/cjce.23632
24. N. Yadav, R. Dhar, S. Mod. Tech, Basics Inst. Appl. (2021). https://doi.org/10.1007/978-981-33-6084-6_19
25. W. Ben Soltan, S. Nasri, M.S. Lassoued, S. Ammar, J. Mater. Sci. Mater. Electron. (2017). https://doi.org/10.1007/s10854-017-6356-1
26. A. Rouahi, A. Kahouli, F. Challali, M.-P. Besland, C. Vallée, B. Yangui, S. Salimy, A. Goullet, A. Sylvestre, J. Phys. D Appl. Phys. (2013). https://doi.org/10.1088/0022-3727/46/6/065308
27. F.I.H. Rhouma, A. Dhahri, N. Farhat, J. Dhahri, K. Khirouni, J. EPJ Web Conf. (2012). https://doi.org/10.1051/epjconf/20122900023
28. C.G. Koops, J. Phys. Rev. (1951). https://doi.org/10.1103/PhysRev.83.121
29. V.R. Palkar, J. John, R. Pinto, J. Appl. Phys. Lett. (2002). https://doi.org/10.1063/1.1458695
30. S. Hcini, A. Omri, M. Boudard, M.L. Bouazizi, A. Dhahri, K. Touileb, J. Mater. Sci. Mater. Electron. (2018). https://doi.org/10.1007/s10854-018-8674-3
31. A. Guerrero, J. Bisquert, G. Garcia-Belmonte, J. Chem. Rev. (2021). https://doi.org/10.1021/acs.chemrev.1c00214
32. M. Mumtaz, M. Naveed, B. Amin, M. Imran, M.N. Khan, J. Ceram. Int. (2018). https://doi.org/10.1016/j.ceramint.2017.12.029
33. K. Ben Brahim, A. Oueslati, M. Gargouri, J. RSC Adv. (2018). https://doi.org/10.1039/C8RA07671E
34. A. Oueslati, J. Ionics. (2017). https://doi.org/10.1007/s11581-016-1878-8
35. S.T. Hameed, T.F. Qahtan, A.M. Abdelghany, A.H. Oraby, J. Mater. Sci. (2022). https://doi.org/10.1007/s10853-022-07134-7
36. K. Ben Brahim, A. Oueslati, F. Hlel, M. Gargouri, J. Mater. Res. Bull. (2019). https://doi.org/10.1016/j.materresbull.2019.110505
37. A.K. Jonscher, J Nat. (1977). https://doi.org/10.1038/267673a0
38. K. Funke, Prog. Solid State Chem. (1993). https://doi.org/10.1016/0079-6786(93)90002-9
39. S.R. Elliott, J. Adv. Phys. (1987). https://doi.org/10.1080/00018738700101971
40. N. Sahu, S. Panigrahi, M. Kar, J. Mater. (2013). https://doi.org/10.1155/2013/802123
41. A.A. Alkathiri, A.A. Atta, M.S. Refat, S. Shakya, A.M. Hassanien, S.A. Algarni, E.M.A. Ahmed, S.E. Alomariy, M. Alsawat, N. Algethami, J. Rare Earths. (2023). https://doi.org/10.1016/j.jre.2022.03.010
42. B.P. Choudhary, N.B. Singh, Bull. Mater. Sci. **39**, 1651 (2016). https://doi.org/10.1007/s12034-016-1329-1
43. L.S. Lobo, A.R. Kumar, J. Non Cryst. Solids. (2019). https://doi.org/10.1016/j.jnoncrysol.2018.11.004
44. A.M. Badr, H.A. Elshaikh, I.M. Ashraf, J. Mod. Phys. (2011). https://doi.org/10.4236/jmp.2011.21004